Materials Advances

ROYAL SOCIETY OF CHEMISTRY

PAPER

View Article Online
View Journal | View Issue



Cite this: *Mater. Adv.*, 2024, 5, 8961

# Rutile-type metal dioxide (110) surfaces for the cyclic oxidation of methane to methanol†

Farrel Dzaudan Naufal, [a] Hasna Afifah,[b] Marleni Wirmas,[b] Mohammad Kemal Agusta,[ac] Adhitya Gandaryus Saputro, [ac] Hadi Teguh Yudistira, [d] Aleksandar Staykov, [e] Kazunari Yoshizawa [f] and Muhammad Haris Mahyuddin *[ac]

Received 15th August 2024,
Accepted 15th October 2024

DOI: 10.1039/d4ma00827h

rsc.li/materials-advances

The direct conversion of methane to methanol has attracted increasing interests, owing to the necessity for an abundant low-carbon source of energy. However, numerous challenges are encountered in attaining a high conversion rate and selectivity using the existing approach and catalysts. One of them is the need for a reaction halt and a reactivation of the catalyst using an oxidant at high temperature, which makes the whole process non-cyclic. In this study, we employ density functional theory calculations to evaluate rutile-type $IrO_2$(110), β-$PtO_2$(110), and β-$MnO_2$(110) surfaces not only for cleaving the H–$CH_3$ bond but also for forming methanol. We find that $IrO_2$(110) and β-$PtO_2$(110) thermodynamically and kinetically favor the C–H activation on the bridging μO-atom terminations *via* a heterolytic pathway. However, the formation of strong Ir–C and Pt–C bonds, which initially help the C–H bond scission, hinders the methanol formation. In the β-$MnO_2$(110) case, in contrast, the Mn–C interaction is quite weak, and the Mn(μ-O)Mn active site is electrophilic, thus allowing the formation of a stable $^{\bullet}CH_3$ radical intermediate state that becomes the driving force for a low-barrier homolytic C–H bond scission as well as a low-barrier and highly exothermic formation of methanol. This first cycle of methane oxidation results in a reduced β-$MnO_2$(110) surface, where no more μ-O active sites are available for the subsequent cycles of methane activation. Nonetheless, this reduced surface can also oxidize methane to methanol when the $H_2O_2$ oxidant is inserted in the mid-way reaction and forms new active sites of μ-OH. The second reaction is also highly exothermic although the C–H activation barrier is not as low as that for the fresh stoichiometric surface. This study suggests the β-$MnO_2$(110) surface as a potential catalyst for the cyclic oxidation of methane to methanol using the $H_2O_2$ oxidant without halting for reactivation.

## 1 Introduction

The utilization of earth-abundant low-carbon methane as a transition to renewable energy sources is highly desirable. However, methane, which is mainly present in natural gas, is difficult to store and transport. Therefore, developing an effective yet efficient means to convert methane to liquids such as methanol is considered essential. Unfortunately, the existing method to convert methane to methanol in industries involves a high-temperature formation of syngas (CO and $H_2$ mixture).[1,2] This approach, however, is not only costly but also inefficient as the resultant CO needs sequential quasi-catalytic treatments to produce methanol.[3,4] In the past decade, the development of heterogeneous catalysts (*e.g.*, metal-exchanged zeolites) for the methane oxidation to methanol had significantly progressed.[5–8] In particular, Fe- and Cu-exchanged zeolites have enabled the reaction to proceed at room temperature,[9–12] which is crucial to reduce costs and more importantly to avoid an overoxidation to products more stable than methanol.[13–15] Accordingly, this has inspired broad development of new catalysts such as single-

[a] *Quantum and Nano Technology Research Group, Faculty of Industrial Technology, Institut Teknologi Bandung, Jl. Ganesha 10 Bandung 40132, Indonesia. E-mail: mahyuddin133@itb.ac.id*
[b] *Doctoral Program of Engineering Physics, Faculty of Industrial Technology, Institut Teknologi Bandung, Jl. Ganesha 10 Bandung 40132, Indonesia*
[c] *Research Center for Nanoscience and Nanotechnology, Institut Teknologi Bandung, Jl. Ganesha 10 Bandung 40132, Indonesia*
[d] *Mechanical Engineering Study Program, Institut Teknologi Sumatera, Way Hui, South Lampung 35365, Indonesia*
[e] *International Institute for Carbon-Neutral Energy Research, Kyushu University, Fukuoka 819-0395, Japan*
[f] *Fukui Institute for Fundamental Chemistry, Kyoto University, Sakyo-ku, Kyoto 606-8103, Japan*

† Electronic supplementary information (ESI) available: Geometrical structure of each reaction step on the stoichiometric surfaces; total DOS of $CH_4$ and $^{\bullet}CH_3$ in the gas phase; energy diagrams of $H_2O_2$ decomposition on the stoichiometric and reduced β-$MnO_2$(110); energy diagram of H–$CH_3$ bond scission on reduced β-$MnO_2$(110) *via* an alternative pathway; energy diagram of $O_2$ dissociation on reduced β-$MnO_2$(110); and CONTCAR files. See DOI: **https://doi.org/10.1039/d4ma00827h**

metal-modified surfaces such as graphene, $CeO_2$, $TiO_2$, ZnO, CuO, *etc.*[16–23]

In these mono/diatomic-dispersed catalysts, however, the methane conversion undergoes the so-called stepwise reaction, where the catalyst must first be activated with $O_2$ or $N_2O$ at high temperature to form the active metal–oxo sites prior to the main reaction of methane oxidation to methanol that takes place at a lower temperature.[24–27] After the first cycle of the reaction, the reaction must then be halted and the reduced catalyst must be reactivated using the same oxidant to continue the reaction to the second cycle and so on. This, consequently, makes the catalysts unpractical for industrial purposes. Attempts to make it more catalytic (*i.e.*, cyclic/continuous reaction) have also been reported, but this approach is less preferred than the stepwise one due to the need for a higher temperature to decompose the oxidant, which accordingly increases the probability for overoxidation to occur and thus gives rise to selectivity issues.[28–31]

In 2017, Liang *et al.*[32] reported that the rutile-type $IrO_2(110)$ surface is highly active for H–$CH_3$ bond scission at temperatures as low as 150 K with an extremely low activation barrier of 0.1 eV. Tsuji and Yoshizawa,[33] by means of density functional theory (DFT) calculations, then elucidated that the $IrO_2(110)$ distorts the geometry of methane (C–H bond elongation and H–C–H angle widening) at the early stage of activation and cleaves the C–H bond in a heterolytic fashion that leads to the formation of a strong Ir–$CH_3$ bond, which explains the high activity of the catalyst. They also suggested β-$PtO_2(110)$ as a catalyst that is more active than $IrO_2(110)$ for the H–$CH_3$ bond scission owing to more geometrical distortions of the adsorbed methane and a stronger Pt–$CH_3$ bond.[33] Despite this, however, an excessively strong metal–$CH_3$ bond would lead to a new challenge when considering the energy required for the metal–$CH_3$ bond cleavage and the following HO–$CH_3$ recombination to form methanol. This is evident from the works by Yeh *et al.*[34] and Martin *et al.*,[35] showing that formaldehyde and $CH_yO_2$, instead of methanol, are two favorable products for methane oxidation on $IrO_2(110)$ in the presence and absence of $O_2$, respectively. Also, Tsuji *et al.*[36] and Takagaki *et al.*[37] have shown that, only through engineering schemes such as nitrogen doping, oxygen defects, and applying supports, β-$PtO_2(110)$ can convert methane to methanol.

In this study, we use DFT calculations to evaluate three rutile-type metal oxide surfaces, including $IrO_2(110)$, β-$PtO_2(110)$, and β-$MnO_2(110)$, not only for catalyzing the methane activation but also for the methanol formation. Being the focus of this study, β-$MnO_2(110)$ is found to easily cleave the H–$CH_3$ bond through a homolytic pathway, where a free $^{\bullet}CH_3$ radical, instead of a Mn–$CH_3$ ligand, is formed as the reaction intermediate, which contrasts the heterolytic mechanism favored by $IrO_2(110)$ and β-$PtO_2(110)$, and becomes the reason for an easy formation of methanol. This paper also discusses the origin of such different mechanisms and the possibility for the reduced β-$MnO_2(110)$ to proceed the second cycle of the reaction by introducing $H_2O_2$ in the mid-way, which renders the catalyst potential for the cyclic (continuous) oxidation of methane to methanol without halting for reactivation.

## 2 Computational details

$IrO_2$, β-$PtO_2$, and β-$MnO_2$ are rutile-type crystals, where the latter two, in particular, have a distorted crystal structure. The optimized bulks were found to have lattice parameters of $a = b =$ 4.522 Å and $c =$ 3.184 Å for $IrO_2$; $a =$ 3.089 Å, $b =$ 4.519 Å, and $c =$ 4.455 Å for β-$PtO_2$; and $a = b =$ 4.474 Å and $c =$ 2.972 Å for β-$MnO_2$. These optimized bulks were then used to construct $5 \times 2$ slab models with nine atomic layers of surface and 15 Å of vacuum for each, a large enough separation to minimize the effect of interactions between the periodically repeated adsorbates. The three topmost atomic layers were allowed to relax in all directions, while the rest were constrained to their optimized positions to represent the bulk.

Spin-polarized calculations were performed using the Kohn–Sham formulation[38,39] as implemented in the Vienna Ab initio Simulation Package (VASP) version 5.4.4.[40,41] The projector augmented wave (PAW) method was employed to describe the interaction between cores and electrons.[42,43] The electron exchange–correlation was treated using the Perdew–Burke–Ernzerhof (PBE)[44] functional based on the generalized gradient approximation (GGA). The plane-wave basis set with a sufficient cut-off energy of 500 eV (Fig. S1, ESI†) was used for all calculations. Considering the large slab models used here, we restricted the Brillouin zone sampling to the $\Gamma$ point only except for PDOS calculations, in which a $3 \times 3 \times 1$ $k$-point mesh was used. The zero-damping D3 method was utilized to account for the dispersion correction.[45] The GGA+$U$ method of Dudarev's simplified rotationally invariant approach[46] was used with $U_{eff}$ values of 7.5 and 5.1 eV, respectively, for the Pt 5d and Mn 3d orbitals, as optimized previously.[33,47,48] The use of different $U_{eff}$ values was tested to insignificantly alter the relative energies (Fig. S2, ESI†). Unlike these two metal orbitals, the Ir 5d orbital exhibits a weak on-site Coulomb interaction of electrons, making the GGA+$U$ treatment unnecessary, consistent with previous studies.[32,33] Due to a great number of metal atoms involved in the present slab surface models, as opposed to the mono/diatomic systems, the spin configuration was not set to a specific spin state. Instead, we let VASP optimize the spin state along with the geometry optimization. Therefore, when the calculations converged, both the geometry and the spin configuration were in the ground state. This is a standard well-accepted method used for many surface systems.[16,33,47–49]

The conjugate gradient method was employed to optimize intermediate structures, while the climbing-image nudged elastic band (CI-NEB) method was used to locate transition states (TSs).[50] The image-dependent pair potential method was used to generate initial images for the CI-NEB calculations.[51] The calculations were considered converged when the maximum forces on the unconstrained atoms are below 0.03 eV $Å^{-1}$. To confirm the presence of a saddle point, vibration frequency calculations were performed using the finite difference method with a small displacement of 0.015 Å. The Bader analysis algorithm[52] was used to calculate atomic spin density, and optimized structures were visualized by using VESTA.[53] The bonding orbital analysis was performed using the projected

crystal orbital Hamilton population (pCOHP) method, as implemented in the LOBSTER package.[54–58]

The surface formation energy ($E_{surf}$) was calculated by using the following formula under the assumption that the surface was formed by cleaving the bulk structure.

$$E_{surf} = \frac{E_{slab} - nE_{bulk}}{2A_{slab}}$$

where $E_{slab}$ and $E_{bulk}$ are the total energies of the slab surface and the bulk, respectively, while $n$ is the ratio of the number of atoms in the slab model to the bulk, and $A_{slab}$ is the surface area of the slab surface. The adsorption energy ($E_{ads}$) of an A molecule is defined as

$$E_{ads} = E_{slab+A} - (E_{slab} + E_A)$$

where $E_{slab+A}$ is the total energy of the slab surface with an adsorbed A molecule and $E_A$ is the total energy of an isolated A molecule. The M–C bond formation energy (M = Ir, Pt, Mn) was calculated by using the following equation, as also used in our previous study:[59]

$$E_{B(M-C)} = E_{slab+CH_3} - (E_{slab} + E_{CH_3})$$

where $E_{slab+CH_3}$ and $E_{CH_3}$ are the total energies of a $CH_3$ ligand adsorbed on the surface M atom and an isolated $^{\bullet}CH_3$ radical, respectively. The O–H bond formation energy was calculated according to the following formula:

$$E_{B(O-H)} = E_{slab+H} - \left(E_{slab} + \frac{1}{2}E_{H_2}\right)$$

where $E_{slab+H}$ and $E_{H_2}$ are the total energies of a single H atom adsorbed on the surface O atom and an isolated $H_2$ molecule, respectively.

# 3 Results and discussion

## 3.1 Stability of the (110) surfaces

In the formation of the (110) surface from rutile-type metal oxides, there are two possible terminations on the topmost layer, namely the O- and M-terminated (110) surfaces (Fig. 1). In these two slab surface models, we have ensured that they consist of symmetrically arranged layers of positive and negative charges, thus exhibiting no net dipole moment perpendicular to the surface normal, which is aligned with the Tasker rules.[60] The calculated $E_{surf}$ shows that the O-terminated surface model for all three studied oxides is easier to form than the M-terminated one. This suggests that the cleavage of $IrO_2$, β-$PtO_2$, and β-$MnO_2$ in a direction perpendicular to [110] tends to form layers covered with two-coordinated bridging O (μ-O) atoms, which is consistent with previous studies.[32,48,61] On the other hand, the M-terminated (110) surface involves one-coordinated dangling O atoms, which makes it less stable. Thus, in the next section, we consider only the O-terminated (110) surface (hereafter referred to as the stoichiometric surface) for evaluating the oxidation of methane to methanol.

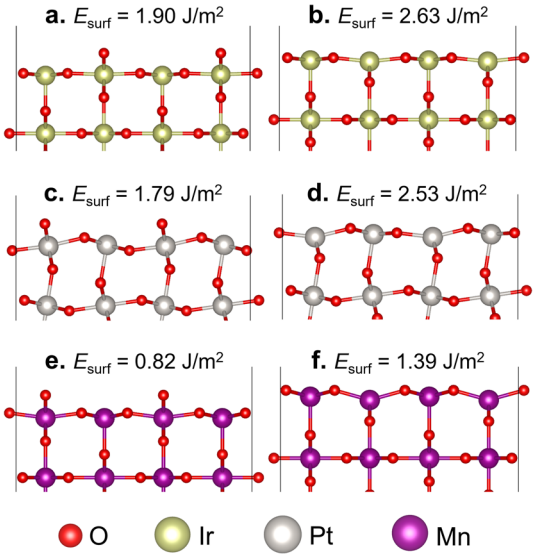


Fig. 1 Optimized slab models of (a) and (b) $IrO_2$(110), (c) and (d) β-$PtO_2$(110), and (e) and (f) β-$MnO_2$(110) surfaces with O-termination (left side) and M-termination (right side). The corresponding $E_{surf}$ (in J $m^{-2}$) is indicated on each slab model.

## 3.2 Methane oxidation on the stoichiometric surface

Here, we consider the bridging μO-atom terminations as the active sites abstracting the H atom of methane and being consumed to form methanol. Another reaction possibility of $H_2O_2$ being introduced together with methane to the surface was also considered. However, in this scenario, $H_2O_2$ decomposes into OOH + μOH (Fig. S3, ESI†), and the following methane reaction with the formed μOH proceeds according to the discussion in section 3.4. Therefore, we first focus our discussion of this section only on the former scenario.

Fig. 2 shows the reaction energy diagrams for all three studied surfaces, while the optimized structures for each reaction step are shown in Fig. S4 (ESI†). The reaction involves three elementary steps, namely methane adsorption, C–H bond activation, and methanol formation. In the first step, as expected, $IrO_2$(110) and β-$PtO_2$(110) strongly adsorb methane with adsorption energies ($E_{ads}$) of −0.75 and −0.65 eV, respectively, whereas β-$MnO_2$(110) weakly adsorbs methane ($E_{ads}$ = −0.22 eV). Looking at the geometry of the adsorbed methane (Fig. 3), we find that only $IrO_2$(110) and β-$PtO_2$(110) are quite close to the adsorbed methane, which is a clear indication of a strong chemical adsorption. This chemisorption forms C–Ir and C–Pt interactions that distort the geometry of methane. As shown in Fig. 3d and e, a significant widening of the ∠H–C–H angle to about 124° and a C–H bond elongation to 1.16 Å are observed, consistent with the previous work of Tsuji and Yoshizawa.[33] In the β-$MnO_2$(110) case (Fig. 3c and f), on the other hand, the weakly adsorbed methane is quite far from the surface and no geometrical distortions are observed (see Fig. 3g for methane geometry in the gas phase), which indicate a physisorption.

In the subsequent C–H activation step, two well-studied pathways (*i.e.*, the homolytic and heterolytic bond scissions that lead to the formation of a $^{\bullet}CH_3$ radical and an M–$CH_3$

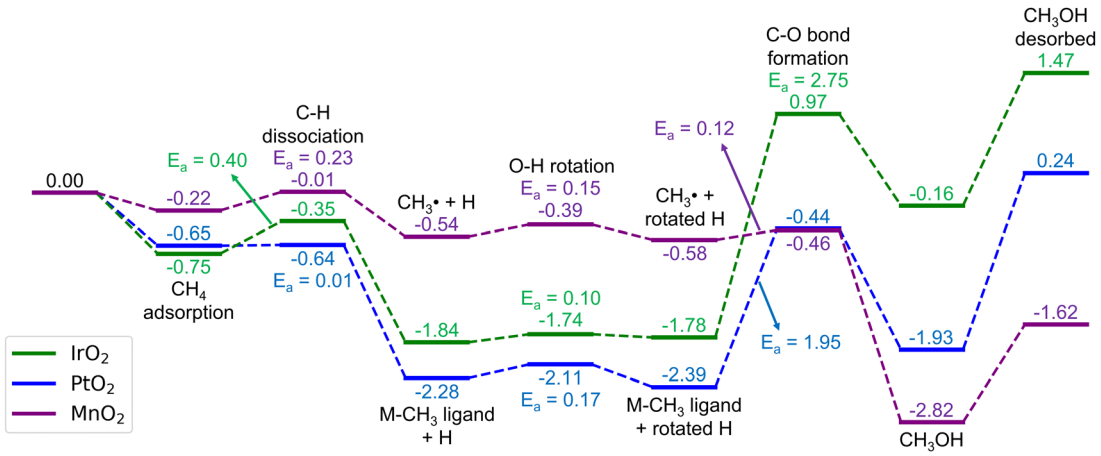


Fig. 2 Energy diagrams (in eV) for the methane oxidation to methanol on the stoichiometric $IrO_2$(110), β-$PtO_2$(110), and β-$MnO_2$(110) surfaces. The corresponding optimized geometries are shown in Fig. S4 (ESI†).

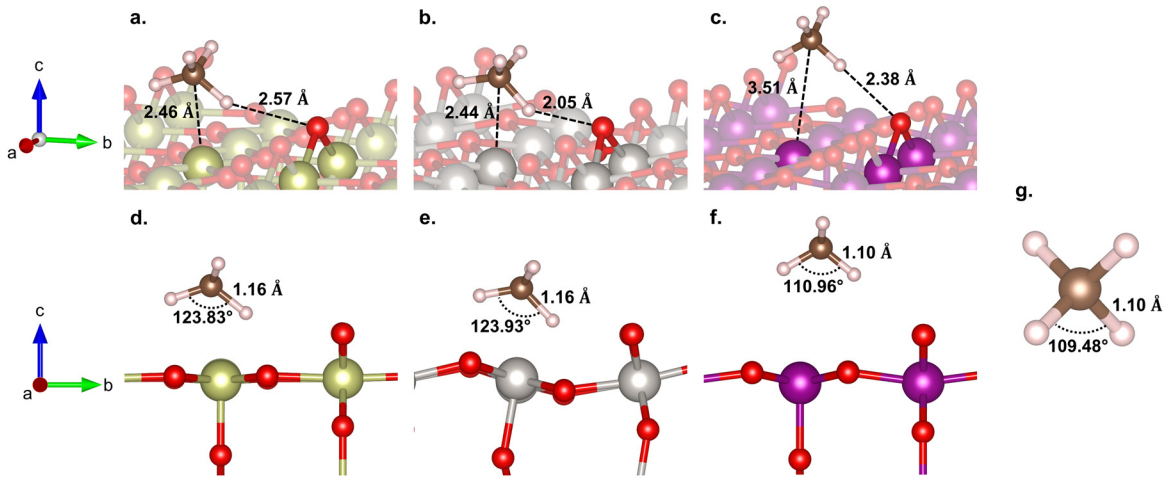


Fig. 3 (top) Side and (bottom) isometric views of methane adsorption on (a) and (d) $IrO_2$(110), (b) and (e) β-$PtO_2$(110), and (c) and (f) β-$MnO_2$(110) surfaces, and (g) the structure of an isolated methane molecule.

ligand intermediate states, respectively) were considered, as many reports also focused on these.[62,63] However, the $IrO_2$(110) and β-$PtO_2$(110) surfaces disfavor the homolytic pathway as the calculations for the formation of the $^{\bullet}CH_3$ radical cannot converge to the minimum required accuracy and eventually forms Ir–$CH_3$ and Pt–$CH_3$ ligands. In contrast, as shown in Fig. 2, the formation of both the $^{\bullet}CH_3$ radical and Mn–$CH_3$ ligand on β-$MnO_2$(110) is favored, enabling us to calculate both the homolytic and heterolytic C–H bond scissions. However, interestingly, after the NEB calculations, we find that the TS structures found for both pathways are similar, which are radical-like TSs. Moreover, the Mn–$CH_3$ ligand formation ($\Delta E$ = −0.51 eV) is found to be slightly less stable than the $^{\bullet}CH_3$ radical formation ($\Delta E$ = −0.54 eV). These clearly indicate that the C–H activation on β-$MnO_2$(110) indeed favors the homolytic pathway.

In terms of energetics, among the studied catalysts, the C–H activation barrier is calculated as the lowest for β-$PtO_2$(110) ($E_a$ = 0.01 eV), the middle for β-$MnO_2$(110) ($E_a$ = 0.23 eV), and the highest for $IrO_2$(110) ($E_a$ = 0.40 eV). It is worth noting that the TSs for β-$PtO_2$(110) and $IrO_2$(110) are more stable than the reference (*i.e.*, methane in the gas phase), suggesting that the actual (apparent) activation barrier for $IrO_2$(110) and β-$PtO_2$(110) might be lower, as also reported by Liang *et al.*[32] In terms of geometry (Fig. 4), the heterolytic C–H bond scission on $IrO_2$(110) and β-$PtO_2$(110) results in a four-centered TS, where the resultant $CH_3^-$ fragment separates from the $H^+$ fragment while interacting with the surface metal atom (M···C distance < 2.31 Å). In contrast, the bond scission on β-$MnO_2$(110) results in a $^{\bullet}CH_3$-like species (*i.e.*, the geometry has not been fully planar yet, but somewhere in between tetrahedral and planar structures) that separates from both the Mn and H atoms and forms an almost planar geometry.

In Fig. 5, the geometries of the M–$CH_3$ ligand and $^{\bullet}CH_3$ radical intermediate states are shown. The Ir–, Pt–, and Mn–$CH_3$ bond lengths are measured to be 2.07, 2.00, and 2.26 Å,

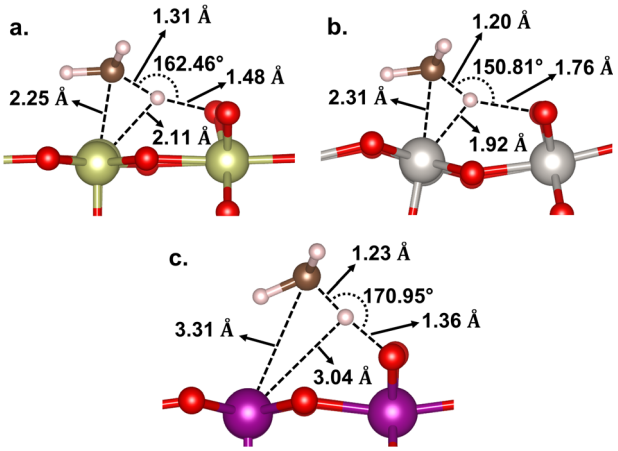


Fig. 4 Geometries of the C–H transition state on (a) $IrO_2$(110), (b) β-$PtO_2$(110), and (c) β-$MnO_2$(110) surfaces.

respectively, which are consistent with their corresponding bond formation energies ($E_{B(M-C)}$ = −2.90, −2.53, and −0.59 eV, respectively). This suggests that the Mn–C bond is so weak that it is not more stable than the $^{\bullet}CH_3$ formation that has a longer Mn···C distance (2.65 Å). Thus, we infer that the methane conversion to methanol on β-$MnO_2$(110) most probably proceeds through an intermediate state of the $^{\bullet}CH_3$ radical without being preceded or succeeded by the Mn–$CH_3$ formation. The formation of the $^{\bullet}CH_3$ radical is indicated by a planar $sp^2$ geometry of $CH_3$ (Fig. 5d) and the presence of a single unpaired electron on the C atom.

The next elementary step is the methanol formation. Here, the $CH_3$ moiety or $^{\bullet}CH_3$ radical recombines with the OH moiety that resulted from the prior methane activation. Other possible pathways such as solvent-assisted methanol formation[15] might also be possible but were excluded from the consideration for the sake of conciseness. To facilitate the HO–$CH_3$ recombination pathway, the OH fragment needs to rotate in a way that the H atom of the OH fragment points outward from the $CH_3$, while the O end of the OH fragment faces toward the $CH_3$, as also

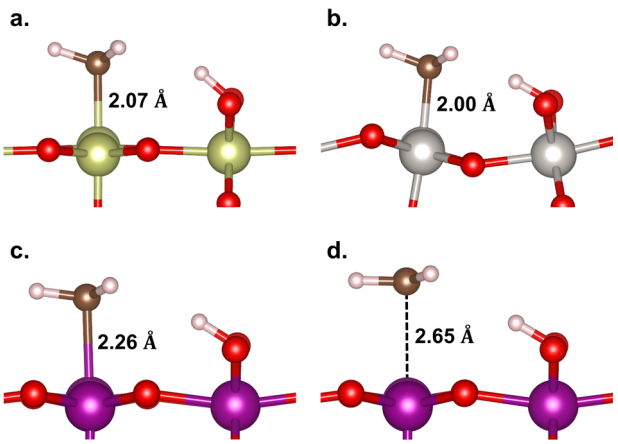


Fig. 5 Geometries of the M–$CH_3$ ligand on (a) $IrO_2$(110), (b) β-$PtO_2$(110), and (c) β-$MnO_2$(110) surfaces, and (d) the $^{\bullet}CH_3$ radical on β-$MnO_2$(110).

considered in our previous studies.[12,20,64] As shown in Fig. 2, this process is found to be low-barrier for all the studied catalysts ($E_a$ = 0.1, 0.17, and 0.15 eV, respectively, for $IrO_2$(110), β-$PtO_2$(110), and β-$MnO_2$(110)).

The recombination between the $CH_3^-$ and the rotated OH on the $IrO_2$(110) and β-$PtO_2$(110) surfaces requires a quite high activation barrier ($E_a$ = 2.75 and 1.95 eV, respectively), the latter of which agrees well with the work of Tsuji *et al.* (2.07 eV).[36] Such a high $E_a$ is as expected from the strong Ir–$CH_3$ and Pt–$CH_3$ bonds that need to be cleaved before the recombination. However, not to our expectation, the formation of methanol chemisorbed on these two surfaces is highly endothermic ($\Delta E$ = 1.62 and 0.46 eV, respectively, for $IrO_2$(110) and β-$PtO_2$(110)). These highly unfavored thermodynamic and kinetic aspects suggest that the methanol formation on these two oxide surfaces is unlikely to happen and, instead, stops at the formation of Ir–$CH_3$ and Pt–$CH_3$ bonds only.

In the β-$MnO_2$(110) case, in contrast, the methanol formation proceeds through a recombination between the $^{\bullet}CH_3$ and OH fragments with a low barrier ($E_a$ = 0.12 eV) and high exothermicity ($\Delta E$ = −2.24 eV). Such a highly favored methanol formation may be attributed to the higher stability of $Mn^{3+}$ ($3d^4$) in the resultant $Mn^{3+}$–$CH_3OH$–$Mn^{3+}$ as compared to $Mn^{4+}$ ($3d^3$) in the $CH_4$ adsorption state. This is also evidenced from the −pCOHP calculations of the methanol formation (Fig. S5, ESI†) showing that the Mn–O antibonding orbital is located at a higher energy than the Ir–O and Pt–O antibonding orbitals, which again indicates that the Mn–O bonds are stronger and thus stabilize the system more significantly. On top of that, β-$MnO_2$(110) also desorbs methanol with a desorption energy (1.20 eV) being the lowest among the three studied catalysts (1.63 and 2.17 eV, respectively, for $IrO_2$(110) and β-$PtO_2$(110)) and comparable to that for the zeolites.[64,65] The geometrical parameters of the methanol adsorbed on the three catalysts are shown in Fig. S6 (ESI†). Fig. S7 (ESI†) shows a good Brønsted–Evans–Polanyi (BEP) relation[66,67] between $E_a$ and $\Delta E$ for HO–$CH_3$ formation, suggesting that a more stable methanol formation requires a lower $E_a$. We have also tried to relate the $E_a$ of HO–$CH_3$ formation to the O p-band center, as suggested by Ge and co-workers.[68,69] However, unfortunately, there seems no high dependency of the HO–$CH_3$ formation on the O p-band center (Fig. S8, ESI†).

We have also evaluated the stability of the formaldehyde ($CH_2O$) and dimethyl ether ($C_6H_2O$) formation as two possible side products of methanol overoxidation. As shown in Fig. S9 (ESI†), two alternative pathways ($CH_{4(g)} \rightarrow CH_2O^* + H_{2(g)}$ and $2CH_{4(g)} \rightarrow C_2H_6O^* + H_{2(g)}$) are considered, and it is found that the formation of $CH_2O$ and $C_6H_2O$ on all studied surface catalysts is much less stable than the methanol formation. This suggests that the overoxidation of methanol is unlikely to occur.

Overall, the reaction on β-$MnO_2$(110) is exothermic ($\Delta E$ = −1.62 eV) with a rate-determining barrier of only 0.23 eV and a highly favorable methanol formation as compared to the $CH_2O$ and $C_6H_2O$ formation. In contrast, the reaction on $IrO_2$(110) and β-$PtO_2$(110) surfaces initially proceeds with a low C–H

barrier but then encounters difficulties in the formation and desorption of methanol with high endothermicity and a rate-determining barrier of >1.9 eV, making them unsuitable for catalyzing the direct conversion of methane to methanol.

### 3.3 Electronic structure analysis

From the discussion above, two questions arise: (1) why does β-$MnO_2$(110) favor the homolytic C–H scission, while $IrO_2$(110) and β-$PtO_2$(110) favor the heterolytic one and (2) why is the $^{\bullet}CH_3$ + OH formation on β-$MnO_2$(110) more stable than the methane adsorption? To answer the first question, we calculate the strength of M–C and O–H bonds formed in the M–$CH_3$ + O–H intermediate state to analyze which of the two contributes more to the stabilization of the intermediate state. As shown in Table 1, the Ir–$CH_3$ binding energy is two times higher than the O–H binding energy, suggesting that the Ir–C bond is extremely strong and thus contributes more to the state stabilization. On β-$PtO_2$(110), on the other hand, both the Pt–$CH_3$ and O–H bonds contribute equally to the stabilization, whereas for β-$MnO_2$(110), the O–H bond contributes predominantly to the formation of the Mn–$CH_3$ + O–H ligand state, indicating that the Mn–C bond is indeed weak. This table, thus, infers that the Ir–C and Pt–C interactions are strong enough to prevent the formation of $^{\bullet}CH_3$ as an intermediate state, making the homolytic C–H bond scission unfavorable for $IrO_2$(110) and β-$PtO_2$(110) surfaces. Also, this suggests that the C–H activation of methane on β-$MnO_2$(110) is driven more predominantly by the O–H bond formation, as also previously suggested by Liu *et al.* for methane activation on metal-zeolites.[70]

Now, to answer the second question, let us analyze the changes of −pCOHP and PDOS during the C–H activation on β-$MnO_2$(110). Fig. 6 shows the −pCOHP values of the dissociated C–H, the formed O–H, and the bridging Mn–O bonds as well as PDOS of the C-p, abstracted H-s, active Mn-d, and bridging O-p orbitals for the adsorption, transition, and intermediate states of methane activation. In Fig. 6a and b, we can see the degenerate $\sigma_{C-H}$ bonding orbitals of methane as they are in the gas phase (see also Fig. S10 (ESI†), only the energy shifts due to the presence of the surface that alters the Fermi level ($E_F$)), indicating a weak adsorbate–surface interaction where the adsorbed methane is undistorted geometrically and electronically. During the homolytic C–H bond scission, the α-electron of the shared electrons in the C–H bond is taken by the H atom, while the β-electron is taken by the C atom. The α electron carried by the H atom is readily transferred to the antibonding Mn–O orbital, as indicated by the presence of a newly formed MnO–H bonding orbital at a low energy (green and orange lines at about −6 eV in Fig. 6c). The β electron, on the other hand, singly occupies the antibonding C-p orbital and forms a free $^{\bullet}CH_3$ radical, as indicated by the presence of an occupied C-p β-orbital and an unoccupied C-p α-orbital in the vicinity of the $E_F$ (blue line in Fig. 6d). After the $^{\bullet}CH_3$ formation, the MnO–H bonding orbital becomes double due to the involvement of two Mn atoms bridging the OH moiety and shifts downward to slightly lower energies (Fig. 6e), indicating that the O–H bond becomes stronger. The unoccupied antibonding C-p α-orbital, on the other hand, shifts upward away from the $E_F$ (Fig. 6f), indicating that the $^{\bullet}CH_3$ is stabilized. Such an electrophilic mechanism, where a transfer of the C–H α-electron leads to a stabilization of the radical intermediate state ($^{\bullet}CH_3$ + O–H) and becomes the driving force for the C–H bond activation, is similar to the $[FeO]^{2+}$-ZSM-5 case.[71] It is worth noting that in the formation of the Mn–$CH_3$ + O–H intermediate state, no electron transfer and redox occur, thus explaining the low stability of the Mn–$CH_3$ and O–H bonds.

Table 1 M–C and O–H binding energies on each studied metal oxide surface

| Metal oxide surface | $E_{B(M-C)}$ (eV) | $E_{B(O-H)}$ (eV) |
|---|---|---|
| $IrO_2$(110) | −2.90 | −1.35 |
| β-$PtO_2$(110) | −2.53 | −2.23 |
| β-$MnO_2$(110) | −0.59 | −2.49 |

### 3.4 Methane oxidation on reduced β-$MnO_2$(110) using the $H_2O_2$ oxidant

Here, we can consider two possibilities of the $H_2O_2$ insertion: (1) being introduced together with methane to the stoichiometric surface, where the $H_2O_2$ decomposition to H + OOH proceeds earlier than the methane activation (Fig. S3, ESI†); or (2) being inserted in the mid-way reaction after a reduced surface is formed due to the consumption of all the μ-O terminations by the prior oxidation of methane ($H_2O_2$ decomposition to 2OH; Fig. S11, ESI†). Whichever the case, the μ-O terminations become μ-OH terminations that now abstract the H atom of methane. Thus, in this section, we focus our discussion on the reduced surface only. As shown in Fig. 7, the $H_2O_2$ decomposes favorably on the reduced β-$MnO_2$(110) surface into 2OH rather than H + OOH (Fig. S11, ESI†). This is possibly due to the absence of the bridging μO-atom terminations that may accommodate the dissociated H atom of $H_2O_2$. Fig. 7 shows that the $H_2O_2$ is first adsorbed on the reduced surface with a rather high $E_{ads}$ of −0.80 eV. The HO–OH bond then dissociates into two OH fragments with a low activation barrier ($E_a$ = 0.04 eV) to form two stable Mn–OH–Mn species with a quite high exothermicity ($\Delta E$ = −3.11 eV).

In the subsequent reaction steps, we consider methane adsorption on the OH-decorated surface, followed by a C–H bond activation *via* the homolytic pathway to directly form methanol. As shown in Fig. 7, the adsorption of methane is rather weak ($E_{ads}$ = −0.22 eV), as also observed previously for the stoichiometric surface (Fig. 2). One H atom of methane is then abstracted in a homolytic fashion with $E_a$ = 1.38 eV and accepted by one of the OH moieties forming a $H_2O$ molecule adsorbed on the surface, while the remaining $CH_3$ fragment forms a free radical species as an intermediate state before the direct formation of methanol takes place. Comparing this to a mechanism where an Mn–$CH_3$ ligand is formed as an intermediate state, instead of $^{\bullet}CH_3$, we find a similar $E_a$ and transition structure (Fig. S12, ESI†), indicating that the homolytic pathway is indeed favored. Moreover, the Mn–$CH_3$ formation ($\Delta E$ = −2.16 eV) is found to be significantly less stable

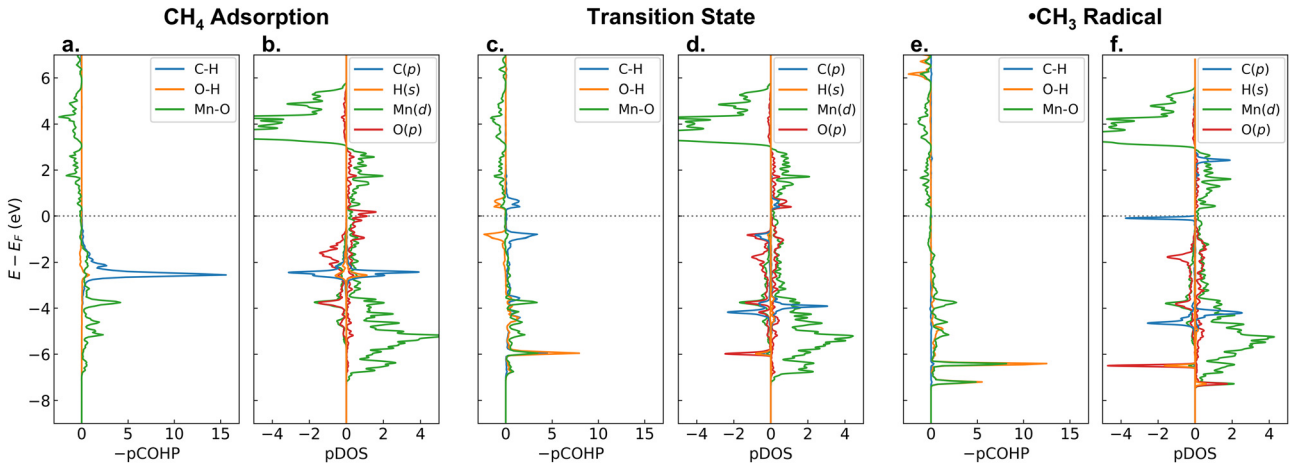


Fig. 6 −pCOHP and PDOS analyses of C–H activation on the β-$MnO_2$(110) surface: (a) and (b) $CH_4$ adsorption state, (c) and (d) transition state, and (e) and (f) $^{\bullet}CH_3$ radical state. Positive and negative −pCOHP values indicate bonding and antibonding interactions, respectively. Positive and negative PDOS values indicate states for the α and β electrons, respectively.

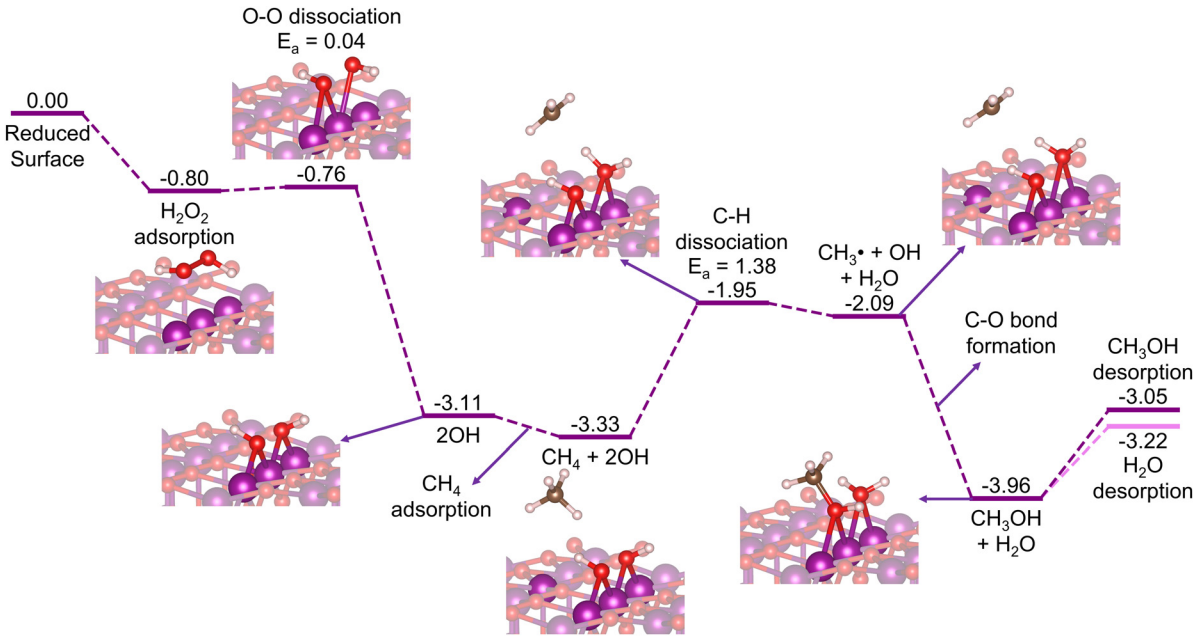


Fig. 7 Energy diagram (in eV) for $CH_4$ oxidation to $CH_3OH$ on the reduced β-$MnO_2$(110) surface with $H_2O_2$ as the oxidation agent.

than the methanol formation ($\Delta E$ = −3.96 eV), suggesting that the $^{\bullet}CH_3$ radical may directly form methanol without forming Mn–$CH_3$ as another intermediate state, as also indicated previously in Fig. 2. The desorption energy of methanol in this case ($E_{des}$ = 0.91 eV) is found to be lower than that in the stoichiometric surface case (1.20 eV). Along with methanol, the formed $H_2O$ molecule also desorbs facilely with an $E_{des}$ of only 0.74 eV, which thus forms the reduced β-$PtO_2$(110) surface again. The subsequent cycles of the $CH_4 + H_2O_2 \rightarrow CH_3OH + H_2O$ reaction can then again proceed repeatedly.

Although the calculated C–H activation barrier for this reduced surface case is much higher than that for the stoichiometric surface case, the overall reaction is downhill and highly exothermic. Furthermore, using $H_2O_2$ as the oxidant allows the reaction to proceed in a cyclic fashion, where $CH_4$ and $H_2O_2$ are introduced together or mid-way continuously to the reactor without halting for reactivation treatments. These suggest that β-$MnO_2$(110), in the form of either an O- or an M-terminated surface, has the potential for oxidizing methane to methanol.

We have also considered $O_2$ as a possible oxidant to form the stoichiometric surface back. Unfortunately, as shown in Fig. S13 (ESI†), the activation energy for the O–O dissociation ($E_a$ = 2.30 eV) is quite high, and the overall reaction is slightly endothermic ($\Delta E$ = 0.06 eV). This suggests that the reduced surface needs to be exposed to a high $O_2$ pressure at elevated temperature to regain the active surface, which is unfavorable

for practical purposes of methane direct conversion to methanol.

## 4 Conclusions

By means of DFT calculations, we have investigated the possibility and mechanism of methane direct oxidation to methanol on three rutile-type metal oxide surfaces, namely $IrO_2(110)$, $\beta$-$PtO_2(110)$, and $\beta$-$MnO_2(110)$. The three catalysts, through their bridging O-atom terminations on the topmost layer, are found to be highly active toward the C–H bond activation ($E_a <$ 0.4 eV). However, only $\beta$-$MnO_2(110)$ can oxidize the resultant $CH_3$ into methanol. Such an ability discrepancy is due to the formation of strong Ir–$CH_3$ and Pt–$CH_3$ bonds during the reaction *via* heterolytic C–H bond scission, consequently increasing the energy required to break the Ir–$CH_3$ and Pt–$CH_3$ bonds and to recombine with the OH ligand. In contrast, for the $\beta$-$MnO_2(110)$ case, the formation of a free $^{\bullet}CH_3$ radical as the reaction intermediate instead of an Mn–$CH_3$ ligand facilitates a direct recombination of OH and $CH_3$ without the need for any prior bond breaking. The ability of $\beta$-$MnO_2(110)$ to form a stable $^{\bullet}CH_3$ radical that drives the reaction to proceed with a low C–H activation barrier owes to the electrophilic nature of the surface.

We have also evaluated the possibility for the reduced $\beta$-$MnO_2(110)$ surface to again oxidize methane to methanol by introducing the $H_2O_2$ oxidant in the mid-way reaction. We find that the $H_2O_2$ facilely decomposes to 2OH, which becomes the new active site for the methane activation. The overall reaction is found to be highly exothermic, and the calculated barrier for the rate-determining C–H activation ($E_a$ = 1.38 eV) is moderate, much lower than the barrier calculated for the rate-determining methanol formation on $IrO_2(110)$ and $\beta$-$PtO_2(110)$. This renders $\beta$-$MnO_2(110)$ potential for catalyzing the $CH_4 + H_2O_2 \rightarrow CH_3OH + H_2O$ reaction in a cyclic fashion.

## Author contributions

F. D. N.: data curation, investigation, methodology, visualization, writing – original draft; H. A.: writing – review & editing; M. W.: writing – review & editing; M. K. A.: supervision, validation, writing – review & editing; A. G. S.: supervision, writing – review & editing; H. T. Y.: writing – review & editing; A. S.: formal analysis, writing – review & editing; K. Z.: writing – review & editing; M. H. M.: conceptualization, funding acquisition, formal analysis, writing – review & editing.

## Data availability

The data supporting this article have been included as part of the ESI.†

## Conflicts of interest

There are no conflicts to declare.

## Acknowledgements

This work was supported by the Indonesia Endowment Fund for Education (LPDP) and Indonesian Science Fund (DIPI) through the RISPRO International Collaboration research scheme (grant no. RISPRO/KI/B1/KOM/11/15539/1/2020). The computations were partly performed at the Research Institute for Information Technology of Kyushu University.

## References

1 J. H. Lunsford, *Catal. Today*, 2000, **63**, 165–174.
2 Z. Zakaria and S. K. Kamarudin, *Renewable Sustainable Energy Rev.*, 2016, **65**, 250–261.
3 H. D. Gesser, N. R. Hunter and C. B. Prakash, *Chem. Rev.*, 1985, **85**, 235–244.
4 H. Schulz, *Appl. Catal., A*, 1999, **186**, 3–12.
5 M. H. Mahyuddin, Y. Shiota, A. Staykov and K. Yoshizawa, *Acc. Chem. Res.*, 2018, **51**, 2382–2390.
6 B. E. R. Snyder, M. L. Bols, R. A. Schoonheydt, B. F. Sels and E. I. Solomon, *Chem. Rev.*, 2018, **118**, 2718–2768.
7 N. F. Dummer, D. J. Willock, Q. He, M. J. Howard, R. J. Lewis, G. Qi, S. H. Taylor, J. Xu, D. Bethell, C. J. Kiely and G. J. Hutchings, *Chem. Rev.*, 2022, **123**, 6359–6411.
8 M. Ravi, M. Ranocchiari and J. A. van Bokhoven, *Angew. Chem., Int. Ed.*, 2017, **56**, 16464–16483.
9 J. S. Woertink, P. J. Smeets, M. H. Groothaert, M. A. Vance, B. F. Sels, R. A. Schoonheydt and E. I. Solomon, *Proc. Natl. Acad. Sci. U. S. A.*, 2009, **106**, 18908–18913.
10 P. Vanelderen, B. E. R. Snyder, M.-L. Tsai, R. G. Hadt, J. Vancauwenbergh, O. Coussens, R. A. Schoonheydt, B. F. Sels and E. I. Solomon, *J. Am. Chem. Soc.*, 2015, **137**, 6383–6392.
11 M. L. Bols, S. D. Hallaert, B. E. R. Snyder, J. Devos, D. Plessers, H. M. Rhoda, M. Dusselier, R. A. Schoonheydt, K. Pierloot, E. I. Solomon and B. F. Sels, *J. Am. Chem. Soc.*, 2018, **140**, 12021–12032.
12 M. H. Mahyuddin, E. T. Lasiman, A. G. Saputro, S. V. Casuarina, N. Nugraha and H. K. Dipojono, *Catal. Sci. Technol.*, 2023, **13**, 5767–5775.
13 M. J. Wulfers, R. F. Lobo, B. Ipek and S. Teketel, *Chem. Commun.*, 2015, **51**, 4447–4450.
14 M. B. Park, S. H. Ahn, M. Ranocchiari and J. van Bokhoven, *ChemCatChem*, 2017, **9**, 3705–3713.
15 M. H. Mahyuddin, S. Tanaka, R. Kitagawa, A. L. Maulana, A. G. Saputro, M. K. Agusta, H. T. Yudistira, H. K. Dipojono and K. Yoshizawa, *J. Phys. Chem. C*, 2021, **125**, 19333–19344.
16 R. K. Singha, Y. Tsuji, M. H. Mahyuddin and K. Yoshizawa, *J. Phys. Chem. C*, 2019, **123**, 9788–9798.
17 Z. Liu, E. Huang, I. Orozco, W. Liao, R. M. Palomino, N. Rui, T. Duchoň, S. Nemšák, D. C. Grinter, M. Mahapatra, P. Liu, J. A. Rodriguez and S. D. Senanayake, *Science*, 2020, **368**, 513–517.
18 X. Cui, H. Li, Y. Wang, Y. Hu, L. Hua, H. Li, X. Han, Q. Liu, F. Yang, L. He, X. Chen, Q. Li, J. Xiao, D. Deng and X. Bao, *Chem*, 2018, **4**, 1902–1910.

19 Y. Qin, H. Liu, L. Li, J. Han, H. Wang, X. Zhu and Q. Ge, *J. Catal.*, 2023, **417**, 323–333.
20 R. P. P. Sukanli, M. H. Mahyuddin, A. G. Saputro, M. K. Agusta, H. T. Yudistira, K. Yoshizawa and H. K. Dipojono, *ACS Appl. Nano Mater.*, 2023, **6**, 6559–6566.
21 Q. Shen, C. Cao, R. Huang, L. Zhu, X. Zhou, Q. Zhang, L. Gu and W. Song, *Angew. Chem., Int. Ed.*, 2020, **59**, 1216–1219.
22 E. Huang, I. Orozco, P. J. Ramírez, Z. Liu, F. Zhang, M. Mahapatra, S. Nemšák, S. D. Senanayake, J. A. Rodriguez and P. Liu, *J. Am. Chem. Soc.*, 2021, **143**, 19018–19032.
23 S. Bai, Y. Xu, P. Wang, Q. Shao and X. Huang, *ACS Catal.*, 2019, **9**, 6938–6944.
24 E. M. C. Alayon, M. Nachtegaal, A. Bodi and J. A. van Bokhoven, *ACS Catal.*, 2014, **4**, 16–22.
25 V. L. Sushkevich, D. Palagin and J. A. van Bokhoven, *Angew. Chem., Int. Ed.*, 2018, **57**, 8906–8910.
26 D. K. Pappas, A. Martini, M. Dyballa, K. Kvande, S. Teketel, K. A. Lomachenko, R. Baran, P. Glatzel, B. Arstad, G. Berlier, C. Lamberti, S. Bordiga, U. Olsbye, S. Svelle, P. Beato and E. Borfecchia, *J. Am. Chem. Soc.*, 2018, **140**, 15270–15278.
27 S. Grundner, M. A. C. Markovits, G. Li, M. Tromp, E. A. Pidko, E. J. M. Hensen, A. Jentys, M. Sanchez-Sanchez and J. A. Lercher, *Nat. Commun.*, 2015, **6**, 7546.
28 K. Narsimhan, K. Iyoki, K. Dinh and Y. Román-Leshkov, *ACS Cent. Sci.*, 2016, **2**, 424–429.
29 J. Xu, R. D. Armstrong, G. Shaw, N. F. Dummer, S. J. Freakley, S. H. Taylor and G. J. Hutchings, *Catal. Today*, 2016, **270**, 93–100.
30 K. T. Dinh, M. M. Sullivan, K. Narsimhan, P. Serna, R. J. Meyer, M. Dincă and Y. Román-Leshkov, *J. Am. Chem. Soc.*, 2019, **141**, 11641–11650.
31 Y. K. Chow, N. F. Dummer, J. H. Carter, C. Williams, G. Shaw, D. J. Willock, S. H. Taylor, S. Yacob, R. J. Meyer, M. M. Bhasin and G. J. Hutchings, *Catal. Sci. Technol.*, 2018, **8**, 154–163.
32 Z. Liang, T. Li, M. Kim, A. Asthagiri and J. F. Weaver, *Science*, 2017, **356**, 299–303.
33 Y. Tsuji and K. Yoshizawa, *J. Phys. Chem. C*, 2018, **122**, 15359–15381.
34 C. H. Yeh, T. M. Le Pham, S. Nachimuthu and J. C. Jiang, *ACS Catal.*, 2019, **9**, 8230–8242.
35 R. Martin, C. J. Lee, V. Mehar, M. Kim, A. Asthagiri and J. F. Weaver, *ACS Catal.*, 2022, **12**, 2840–2853.
36 Y. Tsuji, K. Kurino and K. Yoshizawa, *ACS Omega*, 2021, **6**, 13858–13869.
37 A. Takagaki, Y. Tsuji, T. Yamasaki, S. Kim, T. Shishido, T. Ishihara and K. Yoshizawa, *Chem. Commun.*, 2023, **59**, 286–289.
38 P. Hohenberg and W. Kohn, *Phys. Rev.*, 1964, **136**, B864–B871.
39 W. Kohn and L. J. Sham, *Phys. Rev.*, 1965, **140**, A1133–A1138.
40 G. Kresse and J. Furthmüller, *Comput. Mater. Sci.*, 1996, **6**, 15–50.
41 G. Kresse and J. Furthmüller, *Phys. Rev. B: Condens. Matter Mater. Phys.*, 1996, **54**, 11169–11186.
42 P. E. Blöchl, *Phys. Rev. B: Condens. Matter Mater. Phys.*, 1994, **50**, 17953–17979.
43 G. Kresse and D. Joubert, *Phys. Rev. B: Condens. Matter Mater. Phys.*, 1999, **59**, 1758–1775.
44 J. P. Perdew, K. Burke and M. Ernzerhof, *Phys. Rev. Lett.*, 1996, **77**, 3865–3868.
45 S. Grimme, *J. Comput. Chem.*, 2006, **27**, 1787–1799.
46 S. L. Dudarev, G. A. Botton, S. Y. Savrasov, C. J. Humphreys and A. P. Sutton, *Phys. Rev. B: Condens. Matter Mater. Phys.*, 1998, **57**, 1505–1509.
47 J. A. Dawson, H. Chen and I. Tanaka, *ACS Appl. Mater. Interfaces*, 2015, **7**, 1726–1734.
48 D. A. Tompsett, S. C. Parker and M. S. Islam, *J. Am. Chem. Soc.*, 2014, **136**, 1418–1426.
49 M. H. Mahyuddin, R. V. Belosludov, M. Khazaei, H. Mizuseki and Y. Kawazoe, *J. Phys. Chem. C*, 2011, **115**, 23893–23901.
50 G. Henkelman, B. P. Uberuaga and H. Jónsson, *J. Chem. Phys.*, 2000, **113**, 9901–9904.
51 S. Smidstrup, A. Pedersen, K. Stokbro and H. Jónsson, *J. Chem. Phys.*, 2014, **140**, 214106.
52 G. Henkelman, A. Arnaldsson and H. Jónsson, *Comput. Mater. Sci.*, 2006, **36**, 354–360.
53 K. Momma and F. Izumi, *J. Appl. Crystallogr.*, 2011, **44**, 1272–1276.
54 R. Dronskowski and P. E. Bloechl, *J. Phys. Chem.*, 2002, **97**, 8617–8624.
55 V. L. Deringer, A. L. Tchougréeff and R. Dronskowski, *J. Phys. Chem. A*, 2011, **115**, 5461–5466.
56 S. Maintz, V. L. Deringer, A. L. Tchougréeff and R. Dronskowski, *J. Comput. Chem.*, 2013, **34**, 2557–2567.
57 S. Maintz, V. L. Deringer, A. L. Tchougréeff and R. Dronskowski, *J. Comput. Chem.*, 2016, **37**, 1030–1035.
58 R. Nelson, C. Ertural, J. George, V. L. Deringer, G. Hautier and R. Dronskowski, *J. Comput. Chem.*, 2020, **41**, 1931–1940.
59 M. H. Mahyuddin, A. G. Saputro, R. P. P. Sukanli, F. Fathurrahman, J. Rizkiana, A. Nuruddin and H. K. Dipojono, *Phys. Chem. Chem. Phys.*, 2022, **24**, 4196–4203.
60 P. W. Tasker, *J. Phys. C: Solid State Phys.*, 1979, **12**, 4977.
61 H. Guan, G. Chen, J. Zhu and Y. Wang, *J. Alloys Compd.*, 2010, **507**, 126–132.
62 J. Xu, X. M. Cao and P. Hu, *J. Phys. Chem. C*, 2019, **123**, 28802–28810.
63 A. A. Latimer, H. Aljama, A. Kakekhani, J. S. Yoo, A. Kulkarni, C. Tsai, M. Garcia-Melchor, F. Abild-Pedersen and J. K. Nørskov, *Phys. Chem. Chem. Phys.*, 2017, **19**, 3575–3581.
64 M. H. Mahyuddin, T. Tanaka, Y. Shiota, A. Staykov and K. Yoshizawa, *ACS Catal.*, 2018, **8**, 1500–1509.
65 M. H. Mahyuddin, Y. Shiota and K. Yoshizawa, *Catal. Sci. Technol.*, 2019, **9**, 1744–1768.
66 J. N. Brønsted, *Chem. Rev.*, 1928, **5**, 231–338.
67 M. G. Evans and M. Polanyi, *Trans. Faraday Soc.*, 1938, **34**, 11–24.
68 H. Liu, Y. Qin, L. Li, H. Wang, X. Zhu and Q. Ge, *J. Catal.*, 2024, **431**, 115388.
69 Y. Qin, L. Li, H. Liu, J. Han, H. Wang, X. Zhu and Q. Ge, *J. Chem. Phys.*, 2024, **160**, 134701.
70 C. Liu, G. Li and E. A. Pidko, *Small Methods*, 2018, **2**, 1800266.
71 M. H. Mahyuddin, A. Staykov, A. G. Saputro, M. K. Agusta, H. K. Dipojono and K. Yoshizawa, *J. Phys. Chem. C*, 2020, **124**, 18112–18125.